AIAA JOURNAL
Vol. 32, No. 3, March 1994

Reduction of Blade-Vortex Interaction Noise Through Porous Leading Edge

Soogab Lee*
NASA Ames Research Center, Moffett Field, California 94035

The effect of the porous leading edge of an airfoil on the blade-vortex interaction noise, which dominates the far-field acoustic spectrum of the helicopter, is investigated. The thin-layer Navier-Stokes equations are solved with a high-order upwind-biased scheme and a multizonal grid system. The Baldwin-Lomax turbulence model is modified for considering transpiration on the surface. The amplitudes of the propagating acoustic wave in the near field are calculated directly from the computation. The porosity effect on the surface is modeled in two ways: 1) imposition of prescribed transpiration velocity distribution and 2) calculation of transpiration velocity distribution by Darcy's law. Results show leading-edge transpiration can suppress pressure fluctuations at the leading edge during blade-vortex interaction and consequently reduce the amplitude of propagating noise by 30% at a maximum in the near field.

I. Introduction

A VARIETY of noise sources can be of practical importance for helicopters, and we need to know which ones are dominant and how they depend on design and operating parameters to reduce them. Rotor impulsive noise dominates the region from 250 to 500 Hz, which is most annoying to the human ear, in the far-field noise spectrum of most helicopters. Helicopter impulsive noise can be divided into two categories: 1) high-speed impulsive noise and 2) blade-vortex interaction (BVI) noise. BVI impulsive noise is especially important since it tends to propagate both downward and forward during descending flight near a local airport, whereas high-speed impulsive noise mostly propagates in the forward direction. For a review of helicopter impulsive noise, one should read Schmitz and Yu.[1] To investigate the dominant factors of BVI noise generation and propagation, many experimental, numerical, and theoretical works have been carried out so far. Recently, Booth[2] observed experimentally that the generated noise level strongly depends on steady loading of the blade, miss distance between the blade and a vortex, and vortex structures. Gallman[3] performed a parametric computational study of BVI noise and concluded that tip Mach number, vortex circulation and core size, and miss distance are important in controlling noise strength. In previous works (Lee et al.,[4] Lee and Bershade,[5] and Lee[6]), it was found that the main source mechanism of BVI noise is the formation of an acoustic dipole (pressure fluctuation) near the leading edge, which is caused by the transition of the stagnation point and suction peak (or separation in the strong interaction case) due to the induced velocity by a vortex. In addition, it was found that the leading-edge shape and the thickness of the blade also influence propagating noise amplitudes.

In the present study, the porous leading edge is proposed as a new technique for reducing propagating noise in strong blade-vortex interaction (Fig. 1). Before describing this idea, it might be helpful to review the techniques used until now to reduce impulsive BVI noise during descending flights. Hardin and Lamkin[7] evaluated the critical parameters controlling noise generation, based on the analysis of a simplified two-dimensional, shock-free physical model. Their final expression for the acoustic pressure time history produced by the BVI phenomenon was

$$p(x, t^*) \approx \left(\frac{\Gamma\Gamma_0 U_\infty l}{d^2}\right) = \frac{\Gamma L l}{\rho_\infty d^2} \tag{1}$$

where $t^* = t + x/a_\infty$ is the reception time, x is the observer position in the airfoil-fixed coordinate, l is the length over which the two-dimensional interaction occurs, d is the miss distance, L is the lift per unit length of the airfoil, Γ is the circulation of a vortex, Γ_0 is the bound circulation, and U_∞ and ρ_∞ are the freestream velocity and density, respectively.

The interpretation of the previous equation yields several possibilities for noise reduction. First, the trailing vortex strength can be a possible parameter to control for noise level reduction. It has been attempted to modify shed vortex structure by changing the blade tip shape (e.g., Ogee tip), adding other aerodynamic surfaces (such as winglets), or blowing air along the vortex axis [e.g., tip air mass injection (TAMI)]. These concepts are to spread out and diffuse the vortex so that the BVI is weakened to radiate less noise. The shed vortex strength can also be reduced by actively controlling the pitch angle of the blade [e.g., higher harmonic control (HHC) and individual blade control (IBC)] or the angle of the trailing-edge flap (TEF) at the time of vortex production. The ideas of active control will be discussed later.

Second, the lift per unit length of the blade at the time of interaction can be a parameter, perhaps offering better means of control. This could be reduced by increasing the number of

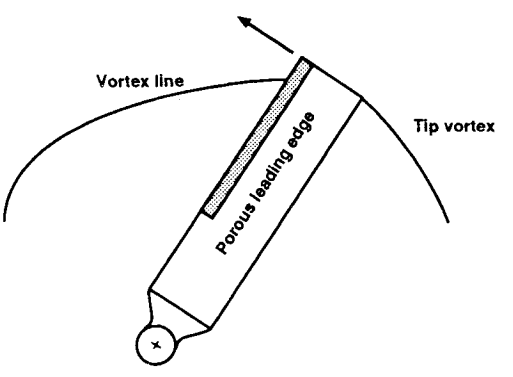

Fig. 1 Illustration of porous leading-edge concept for reduction of BVI noise.

Presented as Paper 93-0601 at the AIAA 31st Aerospace Sciences Meeting, Reno, NV, Jan. 11-14, 1993; received Feb. 17, 1993; revision received June 22, 1993; accepted for publication June 24, 1993.

*Senior Research Specialist, Sterling Federal Systems/U.S. Army Aeroflightdynamics Directorate. Member AIAA.

blades, using longer or wider blades, or reducing the weight of the helicopter. Reducing the weight of the helicopter means reducing the strength of tip vortices. Increasing the number of the blades means increasing the number of interactions, which raises the frequency of BVI and the subjective annoyance levels. Consequently, there is doubt that much success can be achieved with these approaches. Recently, the active control of blade pitch (lift) during BVI was achieved by HHC or IBC[8] to reduce both the shed vortex strength at the time of vortex production and the lift at the time of interaction. These approaches showed potential for BVI noise reduction, even though their effectiveness is coupled with vibration and design complexity.

Third, the interaction length, which is the portion of span over which essentially two-dimensional (parallel) interaction takes place, can be a parameter. The interaction length is usually about 10% of the length of span. This length may be reduced by making the blade curved. As one may expect, a curved blade would be subject to a centripetal force and cause a designer a stability problem.

Last, the miss distance can be a parameter, which is possibly the most influential one. But the miss distance is very difficult to control in the present stage. Recently, active control ideas, namely, TEF[9] and leading-edge flap[10] (LEF), were employed to increase the miss distance at the time of interaction, as well as to decrease the pitch angle of the trailing edge or leading edge (decrease lift) at the time of vortex production.

Some practical attempts based on these ideas can be summarized as follows:

1) TAMI: The TAMI approach consists of injecting a high-pressure jet of air along the axis of the vortex as it leaves the blade tip. The added mass and higher pressure injected into the core cause an instant aging of the vortex. There occurs a rapid radial redistribution of the vorticity accompanied by a more rapid vortex decay due to the higher level of turbulence induced by the jet stream within the vortex core (White and Balcerak[11]). White[12] reported, from model tests, that in the continuously loud banging area the overall sound level was reduced by 7.5 dB(A), whereas in the area of most intense noise, the overall sound was reduced 4.5 dB(A). It was also noted that the primary reduction was in the higher frequencies and not the frequency range that controls the overall sound.

2) Ogee tip: As a passive tip modification, the Ogee tip has been extensively investigated. Researches on the use of the Ogee tip on rotor blades to reduce the impulsive noise and dynamic loads due to blade-vortex interactions are summarized in Ref. 13 and 14. The purpose of the Ogee tip is to redistribute the aerodynamic loading in the tip region where the vorticity shed at the blade tip is more like a vortex sheet than a concentrated line vortex that concentrates the vortex energy in a small compact volume.

The effectiveness of the Ogee tip planform in redistributing pressure and vortex energy can be seen by comparing the pressure data presented by Chigier and Corsiglia[15] for a rectangular tip with the data presented by Balcerak and Feller[16] for the Ogee tip. The comparison showed that the rectangular tip has strong gradients associated with the tip vortex, whereas the Ogee tip showed approximately a two-dimensional pressure distribution over the entire tip region. The flight-test results by Mantay et al.[17] claimed that the use of the Ogee tip altered impulsive BVI noise boundary due to the difference in the loading distribution and provided the pilot with a less noisy descent-approach corridor. They also pointed out that maximum intensity of BVI noise with an Ogee tip was much smaller (by 4 dB) than that with a standard rotor.

3) HHC: A modification of the lift time history of the blade at the time that the incoming vortex is shed from the blade or the blade encounters the shed vortex might be a way to achieve the noise reduction. It is quite apparent that pitch control would modify not only pitch but also the strengths of the shed vortices and possibly the interaction locations. Recently, Brooks et al.[18] and Splettstoesser et al.[19] observed reductions in the amplitude and impulsiveness of noise using higher harmonic pitch control. In both experiments, significant reductions (4–6 dB) were made in the area of the most intense noise for low-speed descent conditions. For other conditions overall noise is almost the same or even increased. In addition, although noise is reduced, this pitch control would generally produce more vibrations, which is undesired in helicopter flight.

4) TEF: The active control of a trailing-edge flap to influence the trajectories of the tip vortex (miss distance) and the strength of the tip vortex was investigated by Hassan et al.[9] Because of the effectiveness of negative flap deflections on the increase of miss distance at interaction and the decrease of vortex strength at production, their results show significant changes of the BVI noise signature and directivity. Average noise reductions of 5 dB with moderate power penalties (58%) were reported.

As a new technique for BVI noise reduction, the effect of leading-edge porosity on the aerodynamic forces and noise propagation during the BVI is investigated. The generic problem of the BVI can be thought of as an unsteady, three-dimensional encounter of a curved line vortex, at an arbitrary intersection angle, with a high-aspect-ratio lifting surface. But, in the present study, the problem is confined to two-dimensional (parallel) BVI in which the intersection angle is zero. In this particular BVI problem with a porous leading edge, Navier-Stokes equations should be solved to resolve the interaction of the boundary layer with a vortex. Especially in cases of strong (or head-on) BVI this is true since the convecting vortex suffers a severe distortion or even division after hitting the leading edge. One difficulty of a Navier-Stokes solver in computing a fluid-flow problem with strong vortices is numerical dissipation. The conventional second-order central or upwind scheme usually has some difficulties in conserving a convecting vortex accurately. Rai[20] introduced a higher fifth-order upwind-biased scheme to overcome numerical dissipation and proved its effectiveness with a high-density grid system.

II. Numerical Procedures

Governing Equations

Consider the unsteady, thin-layer, Navier-Stokes equations in the transformed coordinate system (ξ, η, τ),

$$\tilde{Q}_\tau + \tilde{E}_\xi + \tilde{F}_\eta = R_e^{-1}\tilde{S}_\eta \tag{2}$$

The solution vector $\tilde{Q}$ is given by

$$\tilde{Q} = J^{-1}\begin{pmatrix} \rho \\ \rho u \\ \rho v \\ e \end{pmatrix} \tag{3}$$

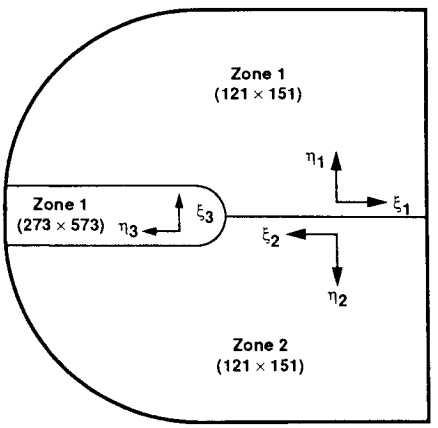

Fig. 2 Patched grid system for the strong blade-vortex interaction.

where ρ is the density, u and v are the velocities in the x and y directions, respectively, and e is the energy per unit volume. Under the independent variable transformation,

$$\begin{aligned} \tau &= t \\ \xi &= \xi(x, y, t) \\ \eta &= \eta(x, y, t) \end{aligned} \tag{4}$$

The inviscid flux vectors $\tilde{E}$ and $\tilde{F}$ are given by

$$\tilde{E} = J^{-1}\begin{bmatrix} \rho U \\ \rho u U + \xi_x p \\ \rho v U + \xi_y p \\ (e+p)U - \xi_t p \end{bmatrix}, \quad \tilde{F} = J^{-1}\begin{bmatrix} \rho V \\ \rho u V + \eta_x p \\ \rho v V + \eta_y p \\ (e+p)V - \eta_t p \end{bmatrix} \tag{5}$$

where p is the pressure. The viscous flux vector is given by

$$\tilde{S} = J^{-1}\begin{bmatrix} 0 \\ K_1 u_\eta + K_2 \eta_x \\ K_1 v_\eta + K_2 \eta_y \\ K_1 K_3 + K_2(u\eta_x + v\eta_y) \end{bmatrix} \tag{6}$$

where

$$\begin{aligned} K_1 &= \mu(\eta_x^2 + \eta_y^2) \\ K_2 &= \mu(\eta_x u_\eta + \eta_y v_\eta)/3 \\ K_3 &= \{Pr^{-1}(\gamma - 1)^{-1}(c^2)_\eta + [(u^2 + v^2)/2]_\eta\} \end{aligned} \tag{7}$$

and μ is the viscosity, Pr is the Prandtl number, and c is the local speed of sound. In these equations, the contravariant velocities along the ξ and η directions are given by

$$\begin{aligned} U &= \xi_t + \xi_x u + \xi_y v \\ V &= \eta_t + \eta_x u + \eta_y v \end{aligned} \tag{8}$$

The metrics η_t, η_x, etc., can be derived from the derivatives of x_τ, x_ξ, etc., using the relations

$$\begin{aligned} \xi_x &= J y_\eta \\ \eta_x &= -J y_\xi \\ \xi_y &= -J x_\eta \\ \eta_y &= J x_\xi \\ \xi_t &= -x_\tau \xi_x - y_\tau \xi_y \\ \eta_t &= -x_\tau \eta_x - y_\tau \eta_y \end{aligned} \tag{9}$$

and J is the transformation Jacobian given by

$$J = \xi_x \eta_y - \xi_y \eta_x = \frac{1}{x_\xi y_\eta - x_\eta y_\xi} \tag{10}$$

The pressure, density, and velocity components are related to the energy per unit volume by the equation of state that is written for a perfect gas as

$$e = \frac{p}{\gamma - 1} + \rho\left(\frac{u^2 + v^2}{2}\right) \tag{11}$$

Numerical Scheme and Grid System

A fifth-order-accurate upwind-biased scheme, based on the Osher type of flux differencing, was used since it is more effective than conventional second-order central or upwind ones in preserving the structure of the convecting vortex correctly against numerical dissipation. The "C" type of multizone grids surrounding the airfoil was used for this calculation, the outer boundaries being approximately 10 chords away in every direction from the center of the airfoil. As seen in Fig. 2, zones 1 and 2 are symmetric, whereas zone 3 is a tubelike region that extends from the leading-edge part of the airfoil to the outer boundary of the region.

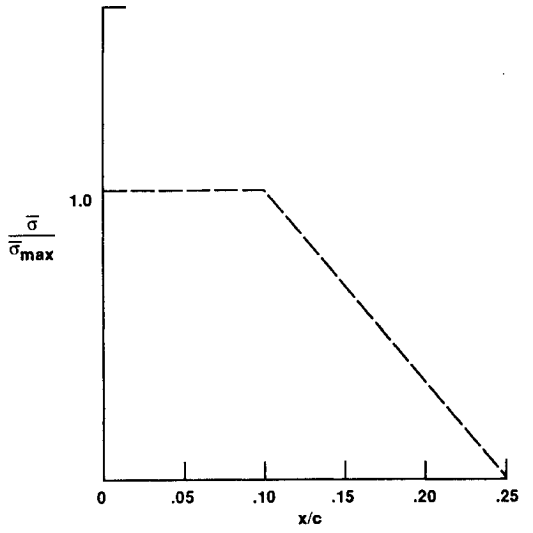

Fig. 3 Distribution of porosity factor along the porous region (from the nose to 25% of the chord).

The reason for using this kind of multizone grid is that we need the high grid density zone (zone 3) for preserving the vortices. However, such large grid point densities are only required in the path of the vortex and in the wake and boundary layers associated with the airfoil. The patched grid method to refine the grid and to minimize the number of grid points required to perform this calculation was developed by Rai and Chaussee.[21] The grids in all three zones were generated by using a combination of algebraic and elliptic grid-generation procedures. The grids are orthogonal to the surface of the airfoil, where zones 1 and 2 are discretized with 121 × 151 grids, and zone 3 is discretized with a 273 × 573 grid, a total of approximately 200,000 grid points.

Vortex Embedding

The analytical expression by Sculley[22] of the tangential velocity of the vortex is given by

$$\frac{v_\theta}{U_\infty} = \frac{\hat{\Gamma}}{2\pi r}\left(\frac{r^2}{r^2 + a_o^2}\right) \tag{12}$$

where a_o and r are the core radius and the distance from the center of the vortex, respectively; both are nondimensionalized by the chord length of the airfoil; and $\hat{\Gamma}$ is defined by the maximum circulation divided by the freestream velocity and the chord length. The sign of the vortex is defined negative in a clockwise flow direction for the vortex in isolation. The pressure and density for the vortex convecting in the freestream are obtained as follows:

$$\frac{dp}{dr} = \frac{\rho v_\theta^2}{r} \tag{13}$$

where the density ρ is obtained from

$$\frac{\gamma p/\rho}{\gamma - 1} + \frac{v_\theta^2}{2} = \frac{\gamma p_\infty/\rho_\infty}{\gamma - 1} \tag{14}$$

Equation (13) is integrated in conjunction with Eq. (14) using a Runge-Kutta scheme. The differential equation is integrated from a large value of r, where the pressure and density are known, inward to the center of the vortex. Equations (13) and (14) represent a stationary vortex that satisfies the steady Euler equations. The vortex is initialized at about three chord lengths ahead of the airfoil by adding this Euler solution of the

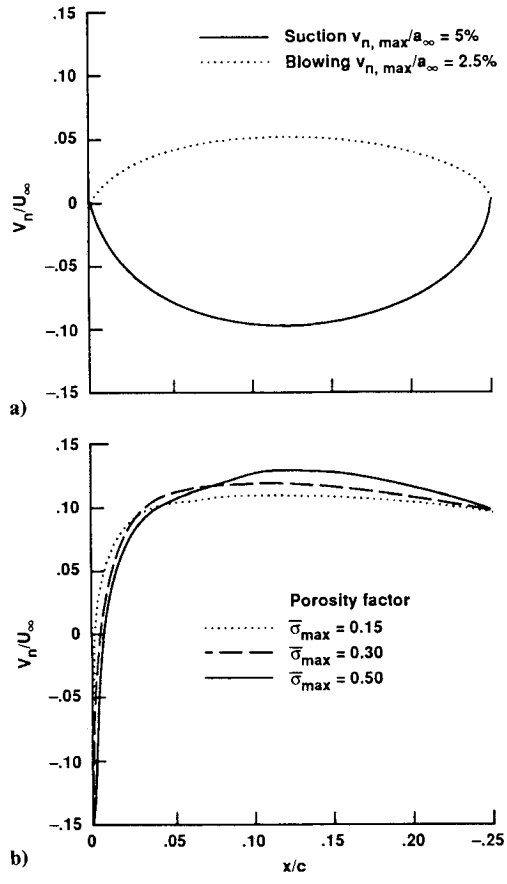

Fig. 4 Transpiration velocity distributions of the porous region (from the nose to 25% of the chord) on both sides of the airfoil for the cases of a) suction on the upper side ($v_{n,max}/a_\infty = 5\%$) where blowing on the lower side ($v_{n,max}/a_\infty = 2.5\%$) and b) porous wall with $\bar{\sigma}_{max} = 0.15$, $\bar{\sigma}_{max} = 0.30$, and $\bar{\sigma}_{max} = 0.50$.

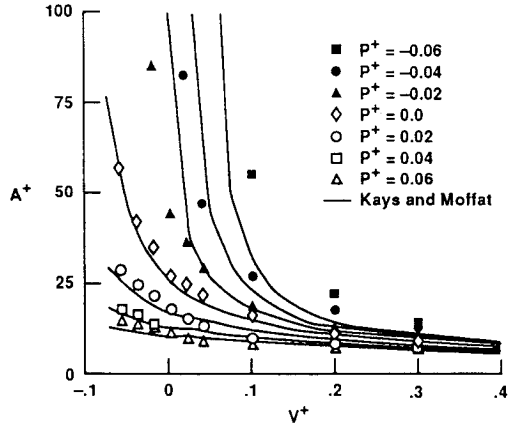

Fig. 5 Dependence of effective sublayer thickness (damping parameter) A^+ on v^+ and p^+.

vortex to the steady-state Navier-Stokes solution of the flowfield. Then the interaction is monitored as the vortex convects with the freestream.

Boundary Conditions

There are three kinds of boundaries in the Navier-Stokes simulation used in this research.

1) The lower boundaries of all three grids correspond to the solid airfoil surface; hence, the no-slip condition and an adiabatic wall condition are imposed at these boundaries. In addition, the derivative of pressure normal to the wall surface is set to zero. All of these conditions and the equations of state together yield

$$\frac{\partial \rho}{\partial n} = 0 \tag{15}$$

$$\frac{\partial e}{\partial n} = u\frac{\partial \rho u}{\partial n} + v\frac{\partial \rho v}{\partial n} \tag{16}$$

where n is the direction normal to the airfoil surface. These boundary conditions are implemented in an implicit manner by using the following equation to update the grid points on the airfoil surface:

$$C(\tilde{Q}_{i,1}^{p+1} - \tilde{Q}_{i,1}^{p}) + D(\tilde{Q}_{i,2}^{p+1} - \tilde{Q}_{i,2}^{p}) = 0 \tag{17}$$

where

$$C = \begin{bmatrix} 1 & 0 & 0 & 0 \\ 0 & 1 & 0 & 0 \\ 0 & 0 & 1 & 0 \\ 0 & \alpha & \beta & 1 \end{bmatrix}$$

$$D = \begin{bmatrix} \theta & 0 & 0 & 0 \\ 0 & 0 & 0 & 0 \\ 0 & 0 & 0 & 0 \\ 0 & \alpha\theta & \beta\theta & \theta \end{bmatrix}$$

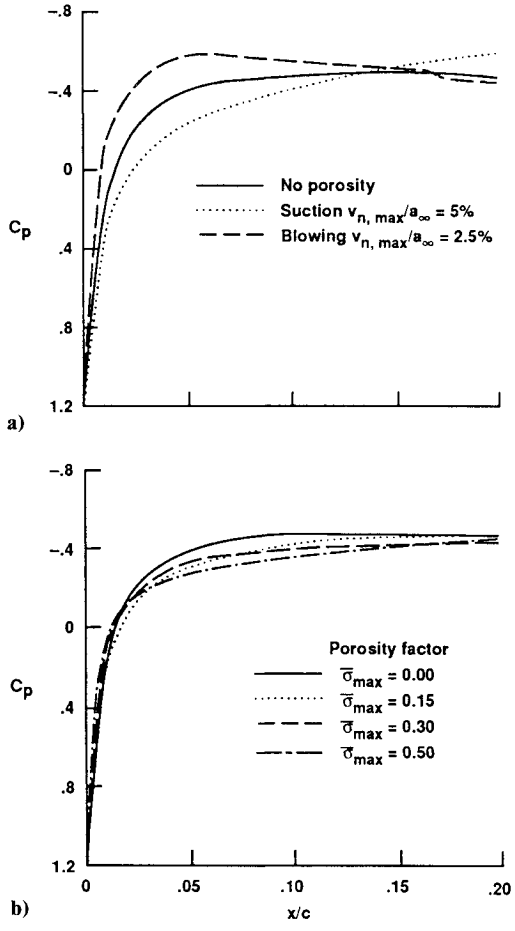

Fig. 6 Steady-state pressure distribution of NACA 0012 with and without transpiration at $M_\infty = 0.5$: a) the blowing and suction with $v_{n,max}/a_\infty = 5\%$ on the upper surface and 2.5% on the lower surface in the region between $x/c = 0.0$ and 0.25, b) porous wall with $\bar{\sigma}_{max} = 0.15$, $\bar{\sigma}_{max} = 0.30$, and $\bar{\sigma}_{max} = 0.50$.

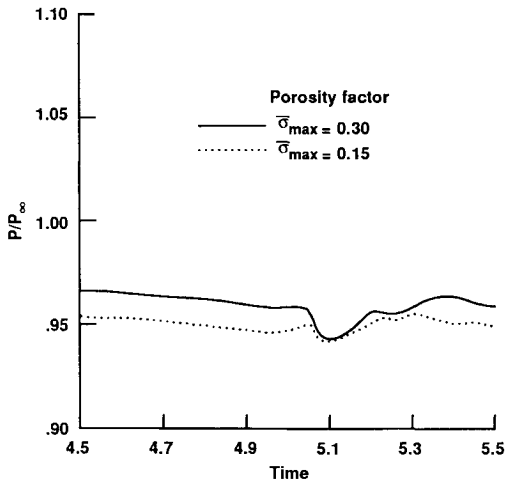

Fig. 7 Time evolution of p_{inner} for the cases of porous wall during BVI.

and

$$\theta = -J_{i,2}/J_{i,1}$$

$$\alpha = -u_{\text{wall}}$$

$$\beta = -v_{\text{wall}}$$

Equation (17) is an implicit, spatially first-order-accurate implementation of the no-slip adiabatic wall condition. A second-order-accurate, three-point, forward-difference corrector step is also implemented after each time step. It should be noted that Eq. (17) requires the grid to be orthogonal at the airfoil surface and the Jacobians of the transformation $J_{i,1}$ and $J_{i,2}$ to be independent of τ.

2) For far-field boundaries of all three zones, the characteristic methods can be used to specify the conditions. Since the upper boundaries $\eta = \eta_{\max}$ are subsonic inlet ones, three quantities need to be specified, and one quantity is extrapolated from the interiors of zones. As we know, for the unsteady two-dimensional case, there are four characteristics and four Riemann invariants. The first three conditions to be specified are the generalized Riemann invariants given by

$$R_1 = \frac{\eta_t + u\eta_x + v\eta_y}{\sqrt{\eta_x^2 + \eta_y^2}} - \frac{2c}{\gamma - 1}$$

$$R_2 = \frac{v\eta_x - u\eta_y}{\sqrt{\eta_x^2 + \eta_y^2}} \tag{18}$$

$$R_3 = \frac{p}{\rho^\gamma}$$

The dependent variables ρ, u, v, and p in Eq. (18) are taken to be the freestream values under the following conditions: the airfoil is at zero angle of attack, and the grid does not contain a vortex. The fourth quantity that is necessary to update the points on this boundary is also a Riemann invariant:

$$R_4 = \frac{\eta_t + u\eta_x + v\eta_y}{\sqrt{\eta_x^2 + \eta_y^2}} + \frac{2c}{\gamma - 1} \tag{19}$$

The right boundary of zone 1 and the left boundary of zone 2 are subsonic exit boundaries. A simple, implicit-extrapolation procedure followed by an explicit, post-update correction is used at these boundaries. The implicit part of the boundary condition for zone 1 is

$$(\tilde{Q}^{p+1}_{i\max,j} - \tilde{Q}^{p}_{i\max,j}) - \frac{J_{i\max-1,j}}{J_{i\max,j}}(\tilde{Q}^{p+1}_{i\max-1,j} - \tilde{Q}^{p}_{i\max-1,j}) = 0 \tag{20}$$

This step is followed by the explicit correction

$$p_{i\max,j} = p_\infty \tag{21}$$

Then the freestream pressure p_∞ is replaced by the pressure corresponding to the composite vortex in a freestream solution if the grid system contains a vortex. In a similar way, the exit boundary of zone 2 is treated. The method for transferring the information in the time-accurate manner across the patch boundaries has been developed by Rai and Chaussee.[21] The last boundary is the wake boundary separating zones 1 and 2. Although the grid lines of zones 1 and 2 are continuous across the wake, for the purpose of convenience the wake boundary is also treated as a patch boundary.

3) For the porous airfoil surface, the blowing (or suction) velocity v_n is specified or calculated, and the tangential velocity is set to zero. The pressure boundary condition at the airfoil surface is taken to be $\partial p/\partial\eta = 0$, since the η coordinate lines are orthogonal to the airfoil, and the grids are very fine in the η direction near the airfoil surface. The adiabatic wall condition and the equation of state are also used. Since the holes in the porous region are very small and close together, it is difficult to compute the flow across the porous media without extremely fine grids. Therefore, in the present study the porosity effect is modeled in two ways instead of being computed.

Porosity Modeling

First, transpiration velocity is predetermined along the porous wall. When a negative (clockwise) vortex strongly interacts with the leading edge, which is the case in this study, the leading-edge portion of the airfoil receives a temporary negative force (nose down) since the stagnation region moves to the upper part where a lower pressure region is made on the lower part. To reduce this unsteady loading due to interaction with vortices, one may think of a method to apply an inverse force on the nose part of the airfoil, which is an idea of active control. This might help to suppress pressure fluctuations near the leading edge and result in reducing the magnitudes of the propagating noise. This idea can be achieved by suction on the upper part of leading edge and blowing on the lower part. The blowing (or suction) velocity is specified by

$$v_n = v_{n,\max}\sqrt{\sin\frac{x - x_1}{x_2 - x_1}\,\pi} \tag{22}$$

Suction on the upper surface is given with $v_{n,\max}/a_\infty = 5\%$ where blowing on the lower surface with $v_{n,\max}/a_\infty = 2.5\%$ in the porous region from $x_1/c = 0.0$ to $x_2/c = 0.25$. The distribution of blowing (or suction) velocity is shown in Fig. 4a. This case is referred to as blowing and suction hereafter.

Second, transpiration velocity is determined by the pressure differences between the porous wall. The model proposed is based on Darcy's law[23] such that

$$v_n = -\frac{\bar{\sigma}}{\rho_\infty U_\infty}(p_{\text{outer}} - p_{\text{inner}}) \tag{23}$$

where the subscript outer means the outer-flow property and inner indicates the inner property of the cavity; $\bar{\sigma}$ is the porosity factor, which is determined by viscosity, as well as by the size and spacing of the holes in the porous surface. Along the porous wall, the porosity factor is distributed as follows (Fig. 3):

$$\begin{aligned} \bar{\sigma} &= \sigma_{\max} \qquad 0.0 < x/c < 0.1 \\ \bar{\sigma} &= -\frac{\sigma_{\max}}{3}[20(x/c) - 5] \qquad 0.1 \le x/c \le 0.25 \end{aligned} \tag{24}$$

In this study the values of $\bar{\sigma}_{max}$ were selected to be 0.15, 0.30, and 0.50. For simplicity, uniform pressure is assumed inside the cavity (without calculating the detailed flow motion), that is,

$$p_{inner} = f(\text{time}) \text{ only} \tag{25}$$

For the transpired flow through the cavity, the net mass flow through the porous surface of length S must be zero. This condition can be written as

$$Q = \int_S \rho v_n \, ds = 0 \tag{26}$$

which gives to the expression of mass-averaged pressure in the cavity

$$p_{inner} = \frac{\int_S \bar{\sigma}(\rho p)_{outer} \, ds}{\int_S \bar{\sigma}\rho \, ds} \tag{27}$$

This uniform cavity pressure assumption was made for convenience but is expected to be qualitative accurate even though accurate calculation of the flow in the cavity is desirable. The resultant distributions of transpiration velocity with $\bar{\sigma} = 0.15$, 0.3, and 0.5 are shown in Fig. 4b. With a porous leading edge, the airfoil experiences a suction up to 3 or 4% of the chord length, and after that point, it has a blowing up to the quarter chord. This effect is increased with the porosity factor.

Turbulence Model

Baldwin-Lomax turbulence model[24] used in this calculation was patterned after that of Cebeci-Smith, with modifications that make it unnecessary to find the outer edge of the boundary layer. However, the Baldwin-Lomax turbulence model did not consider the blowing (or suction) effect on the damping parameter A^+. The modification on A^+, originally proposed by Launder and Priddin,[25] is selected for taking transpiration at the surface into account. In this model, the modified damping factor is expressed as

$$A^+ = \frac{26}{(\tau^+)^n} \tag{28}$$

and τ^+ is defined as

$$\tau^+ = 1 + p^+ y^+ + v^+ u^+ \tag{29}$$

where

$$\tau^+ = \frac{\tau}{\tau_w}$$

$$p^+ = \left(\frac{dp}{dx}\right)\left(\frac{\nu}{\rho u_\tau^3}\right)$$

$$y^+ = \frac{\rho_w u_\tau y}{\mu_w} = \frac{\sqrt{\rho_w \tau_w} y}{\mu_w}$$

$$v^+ = \frac{v_n}{u_\tau}$$

$$u^+ = \frac{\bar{u}}{u_\tau}$$

$$u_\tau = \sqrt{\tau_w/\rho_w}$$

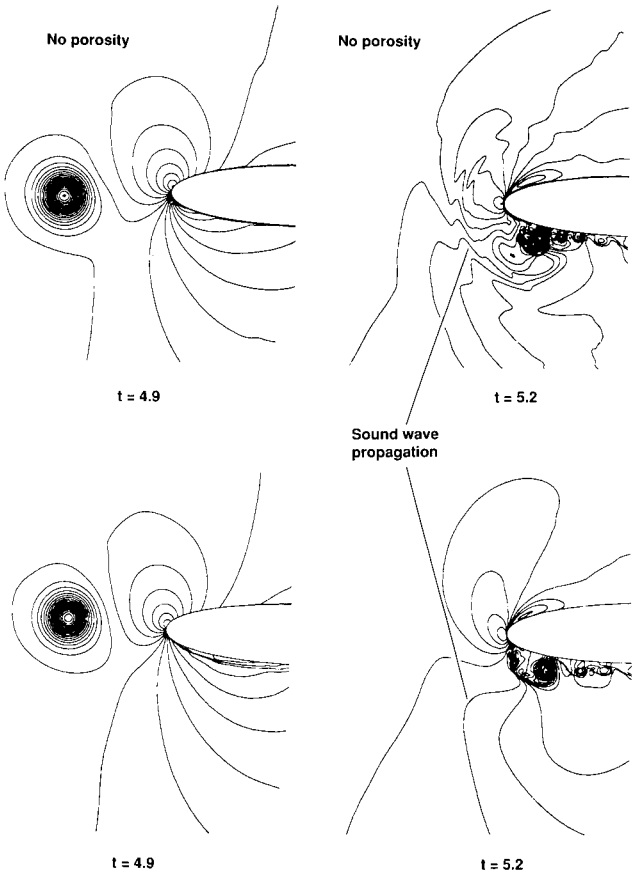

Fig. 8 Comparison of density contour developments during BVI (at time = 4.9 and 5.2) without and with porosity ($\bar{\sigma}_{max} = 0.15$).

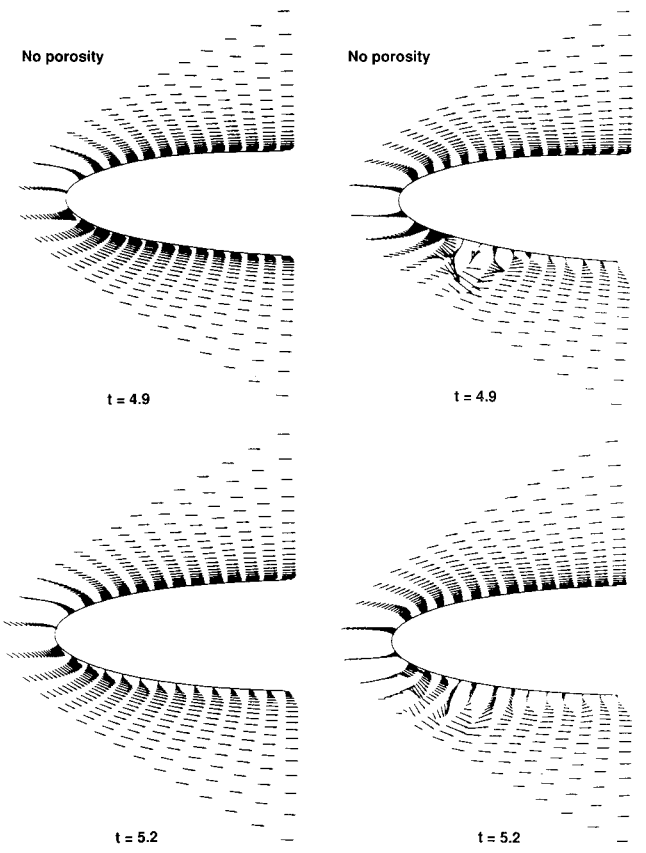

Fig. 9 Velocity profiles near the porous region (up to $x/c = 0.25$) during BVI (at time = 4.9 and 5.2) without and with porosity ($\bar{\sigma}_{max} = 0.15$).

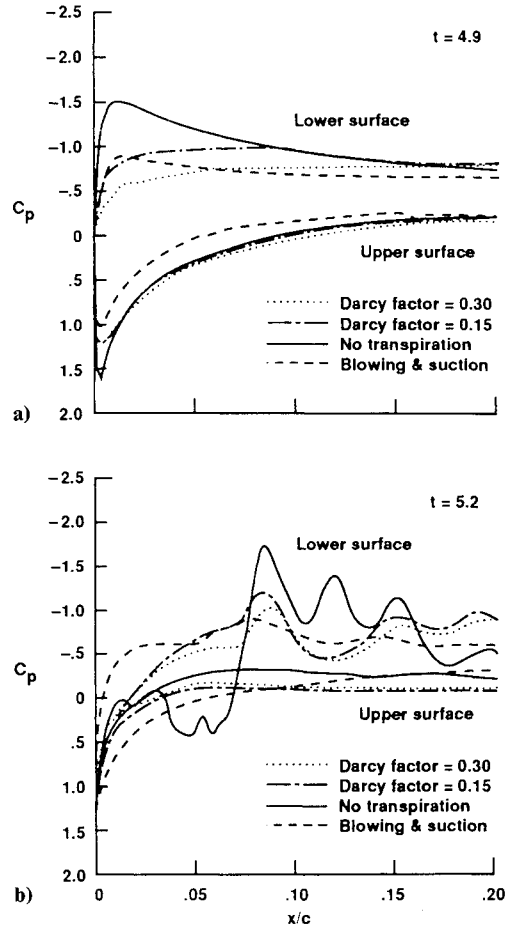

Fig. 10 Comparison of surface pressure developments during BVI (at time = 4.9 and 5.2) without and with transpiration: a) blowing and suction, b) porous wall with $\bar{\sigma}_{max} = 0.15$ and 0.30.

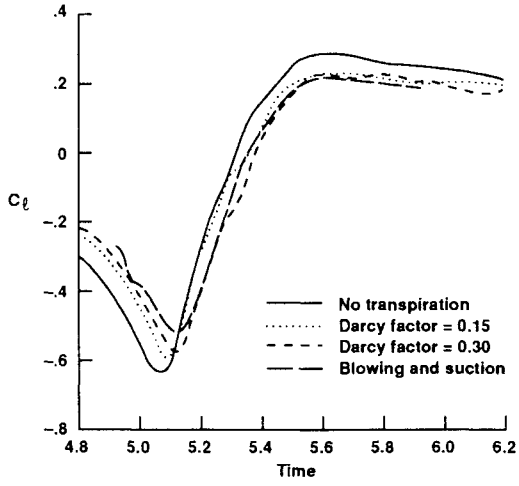

Fig. 11 Comparison of lift coefficient variations during BVI without and with transpiration: a) blowing and suction, b) $\bar{\sigma}_{max} = 0.15$ and 0.30; conditions: $M_\infty = 0.5$, $\Gamma = 0.28$, and $a_o/c = 0.02$ ($y_{v_o}/c = 0.20$ at $x_{v_o}/c = -1.1$).

In Eq. (28), the value of n is in the range proposed by several researchers such as Patankar and Spalding[26] ($n = 0.5$), Kays and Crawford[27] ($n = 0.5$) based on experimental data by Andersen et al.,[28] Chen et al.[29] ($n = 0.7$), Baker et al.[30] ($n = 1.0$), and Launder and Priddin[25] ($n = 1.7$). In this study, the value was selected as 0.7.

The A^+ represents simply an effective viscous sublayer thickness, which is apparently influenced by pressure gradient, transpiration, and surface roughness. The surface roughness is not considered in the present study, even though it severely decreases A^+. The modification in Eq. (28), added to the Baldwin-Lomax turbulence model, yields higher skin friction values in the blowing region than those calculated by the original Baldwin-Lomax model. Conversely, it predicts the skin friction in the suction region that is lower than that from the original model. This is because in the modified version the blowing increases the mixing rate (A^+ being decreased), and the suction tends to laminarize the flow (A^+ being increased). As an alternative model to calculate A^+ with transpiration, Kays and Moffat[31] introduced an empirical formula:

$$A^+ = \frac{25.0}{a\{v^+ + b[p^+/(1 + cv^+)]\} + 1.0} \tag{30}$$

where $a = 7.1$, $b = 4.25$, $c = 10.0$; if $p^+ > 0.0$, $b = 2.9$, $c = 0.0$; and if $v^+ < 0.0$, $a = 9.0$.

Figure 5 shows the comparison of the model used in this calculation and the model by Kays and Moffat. Results tend to be well matched in the region of adverse pressure gradient. In the region of favorable pressure gradient, some discrepancies are shown.

III. Steady-State Solution

In this study, Mach number and Reynolds number were selected to be 0.5 and 1.29×10^6, respectively. The circulation ($\Gamma/U_\infty c$) and core size (a_o/c) of the convecting vortex were chosen to be 0.28 and 0.02, respectively; c denotes the airfoil chord length. Figures 6a and 6b display the steady-state surface pressure distributions with the two types of transpiration model mentioned earlier.

In Fig. 6a, the blowing on the lower porous region (from the nose to the quarter chord) induces higher pressure than that of the no-blowing case. Conversely, the suction at the upper surface induces lower pressure than that of the no-suction case. Applying this type of blowing and suction on the leading edge results in positive force (nose-up pitching moment) at the nose part. In the case of a porous wall, shown in Fig. 5b, the stagnation pressure is a little bit decreased, and after 2% of the chord, the airfoil has higher values of pressure than those of the no porosity case. It is also shown that this effect is enhanced as the porosity factor is increased.

IV. BVI and Noise Propagation

Figure 7 represents the time history of the cavity pressure during the strong (head-on) BVI. The inner pressures of both cases decrease slightly up to time = 5.0 (approximately at this time the vortex hits the leading edge) and later experience

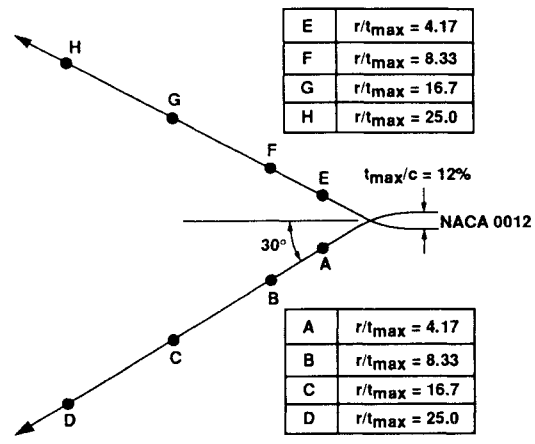

Fig. 12 Selected (airfoil-fixed) observation points at the acoustic near field.

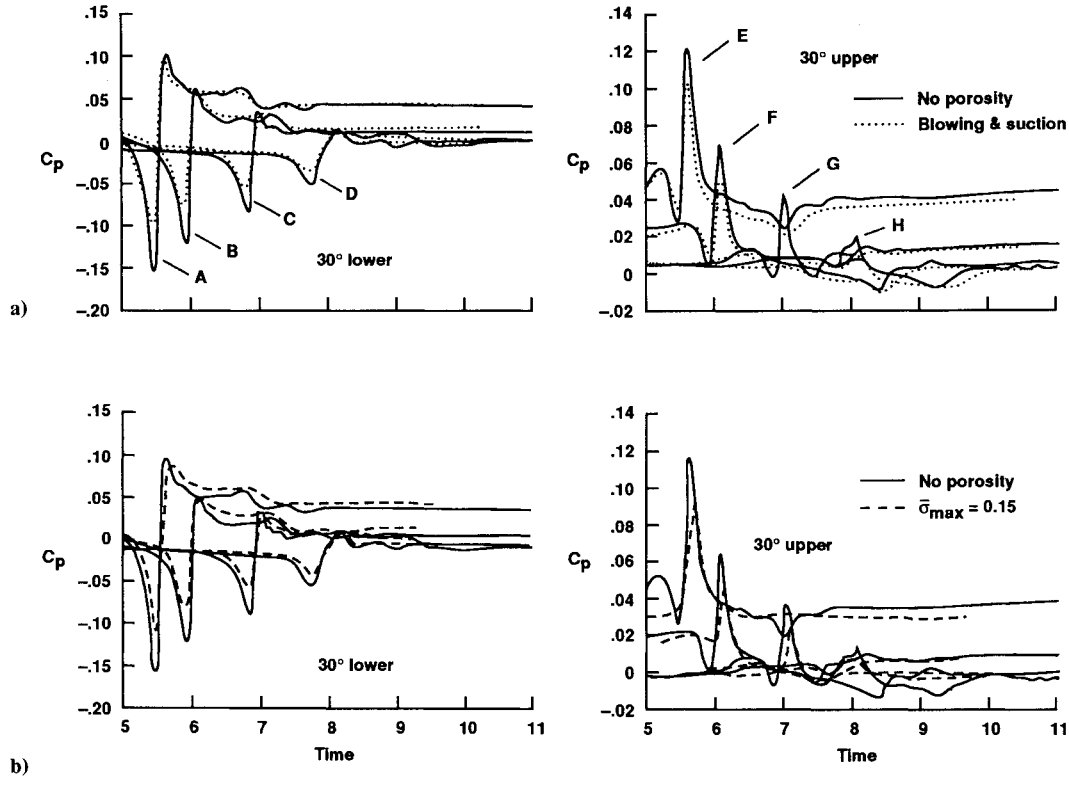

Fig. 13 Comparisons of near-field noise signatures with and without transpiration at $M_\infty = 0.5$: a) the blowing and suction with $v_{n,max}/a_\infty = 5\%$ on the upper surface and 2.5% on the lower surface, b) the porous wall with $\bar{\sigma}_{max} = 0.15$.

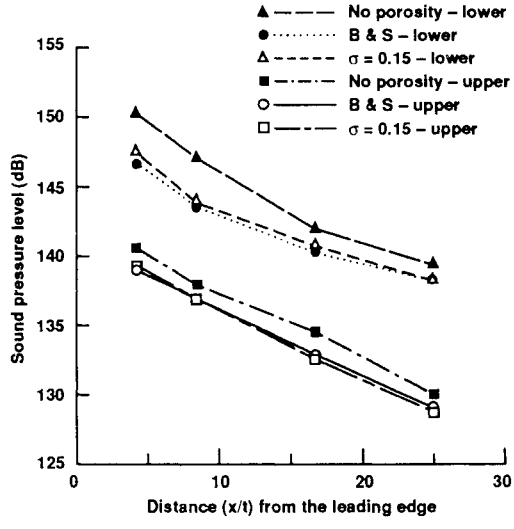

Fig. 14 Comparisons of sound pressure level with and without transpiration at $M_\infty = 0.5$: a) the blowing and suction with $v_{n,max}/a_\infty = 5\%$ on the upper surface and 2.5% on the lower surface, b) the porous wall with $\bar{\sigma}_{max} = 0.15$.

some fluctuations whose magnitudes are 3% of ambient pressure at maximum. Figure 8 compares the density contour evolutions with and without porosity ($\bar{\sigma}_{max} = 0.15$) at the times right before ($t = 4.9$) and after ($t = 5.2$) the vortex hits the leading edge. (Time is nondimensionalized by U_∞/c and $t = 0$ when the vortex is located at 5 times chord length ahead of the leading edge.) The figures at $t = 5.2$ clearly show that the case with porosity produces a much weaker acoustic wave than that with no porosity. In Fig. 9, the velocity vectors near the porous region at the time of 4.9 and 5.2 are compared with those of the no-porosity case. With $\bar{\sigma}_{max} = 0.15$, the boundary layer at the upper surface becomes thinner than that without porosity and vice versa at the lower surface. At $t = 5.2$, it can be noticed that the vortex of the case with $\bar{\sigma}_{max} = 0.15$ is weaker than that of the no-porosity case due to the interaction with the transpired boundary layer.

Figure 10 displays the distributions of surface pressure at the times of 4.9 and 5.2. Three cases with transpiration are compared with the case of no porosity. In Fig. 10a, the no-porosity case displays a typical *Cp* distribution with a pressure peak on each of the surfaces (positive on the upper surface and negative on the lower surface) slightly behind the leading edge. These pressure peaks are relaxed to the forward after the vortex passes by the airfoil, and they become a source of noise propagation (see Lee[6]). This figure also shows that all three cases with porosity show lower pressure peaks than those of no porosity on both the upper and lower surfaces, which implies weaker noises. At $t = 5.2$ (Fig. 10b), no pressure peak is shown near the leading edge since it is relaxed. In Fig. 11, the comparison of lift coefficient developments with and without porosity during BVI is shown. Lift variation of the cases with porosity shows 10–20% reduction in amplitudes with slight decreases of the slope. The blowing and suction case shows a weaker lift variation than those of the porous wall cases. It is worthwhile to note that the case with $\bar{\sigma}_{max} = 0.30$ has a little bit smaller lift variation than that with $\bar{\sigma}_{max} = 0.15$.

Eight selected observation stations in the near field of the airfoil are shown in Fig. 12. These points are fixed with the airfoil, that is, the observer moves with the airfoil. Four points are sitting on the 30-deg upper line from the leading edge where the other four are on the 30-deg lower line. The airfoil maximum thickness ($a = t_{max}$), rather than the chord length, is used as a reference length since BVI phenomenon is concentrated on the leading-edge part. In Figs. 13a and 13b, the acoustic waveform propagations of the blowing and suction case and the $\bar{\sigma}_{max} = 0.15$ case are compared with the baseline (no-porosity) result. In these figures, the solid lines represent

the case of no transpiration at the leading edge where the dotted lines represent the case of transpiration. The acoustic wavelength λ approximately corresponds to 15 times the maximum thickness of the airfoil. Estimation of Helmholtz number shows that this case ($wa/c \approx 1/2$) lies between compact ($wa/c \ll 1$) and noncompact ($wa/c \gg 1$) cases. The comparison shows that the peak amplitudes of waves are reduced approximately by 20 ~ 30% in both transpiration cases. The sound pressure level (SPL) at the near-field observation points of the cases with porosity are also compared with the no-porosity case in Fig. 14. Results indicate that both cases (the blowing and suction case and the $\bar{\sigma}_{max} = 0.15$ case) have approximately 2 dB reduction at the observation position of $r/t_{max} = 25.0$.

V. Summary and Conclusions

The present study demonstrates the effect of leading-edge porosity on the propagation of acoustic waves due to BVI. A thin-layer Navier-Stokes two-dimensional solver, with a highly fine multizonal grid and a higher order upwind-biased scheme, is employed to calculate a near-field solution of BVI acoustics with an airfoil-fixed coordinate. A modified Baldwin-Lomax turbulence model is selected to consider the transpiration at the surface. Porosity at surfaces is modeled in ways of specifying or calculating the normal velocity at the wall. Results show that the porosity at the leading edge, in a case of strong head-on BVI, can reduce the near-field noise propagation up to 20–30%. This effect is due to the suppression of the strength of pressure fluctuations near the leading edge during BVI by exchanging mass and momentum through the surface.

Acknowledgments

The author wishes to thank M. M. Rai, NASA Ames Research Center, for providing his BLADE code and valuable comments. Useful suggestions of C. Tung and Y. H. Yu, U. S. Army Aeroflightdynamics Directorate at NASA Ames Research Center, are also gratefully acknowledged, as are discussions with D. Bershader, Stanford University.

References

[1]Schmitz, F. H., and Yu, Y. H., "Helicopter Impulsive Noise: Theoretical and Experimental Status," *Recent Advances in Aeroacoustics*, edited by A. Krothapalli and C. A. Smith, Springer-Verlag, New York, 1986, pp. 149–243.

[2]Booth, E. R., "Experimental Observations of Two-Dimensional Blade-Vortex Interaction," *AIAA Journal*, Vol. 28, No. 8, 1990, pp. 1353–1359.

[3]Gallman, J. M., "A Parametric Computational Study of Isolated Blade-Vortex Interaction Noise," DGLR/AIAA 14th Aeroacoustics Conference, AIAA Paper 92-02-119, Aachen, Germany, May 1992.

[4]Lee, S., Bershader, D., and Rai, M. M., "An Experimental and Computational Study of 2-D Parallel Blade-Vortex Interaction," AIAA Paper 91-3277, Sept. 1991.

[5]Lee, S., and Bershader, D., "On Head-On Parallel Blade-Vortex Interaction," *AIAA Journal*, Vol. 32, No. 1, 1994, pp. 16–22.

[6]Lee, S., "Strong Parallel Blade-Vortex Interaction and Noise Propagation in Helicopter Flight," Ph.D. Thesis, Dept. of Aeronautical and Astronautical Engineering, Stanford Univ., Stanford, CA, June 1992.

[7]Hardin, J. C., and Lamkin, S. L., "Concepts for Reduction of Blade-Vortex Interaction Noise," *Journal of Aircraft*, Vol. 24, No. 5, 1986, pp. 120–125.

[8]Ham, N. D., "Helicopter Individual-Blade-Control and Its Applications," *Proceedings of the American Helicopter Society 39th Annual Forum* (St. Louis, MO), May 1983, pp. 613–623.

[9]Hassan, A. A., Charles, B. D., Tadghighi, H., and Sankar, L. N., "Blade-Mounted Trailing Edge Flap Control for BVI Noise Reduction," NASA CR 4426, Feb. 1992.

[10]Wang, C. M., Tung, C., and Yu, Y. H., "A Numerical Study of Airfoil Deformation in Vortex-Airfoil Interaction Problems," AIAA Paper 93-3287, Oct. 1993.

[11]White, R. P., and Balcerak, J. C., "An Investigation of the Mixing of Linear and Swirling Flows," RASA Rept. 72-04, Feb. 1972.

[12]White, R. P., "Wind Tunnel Tests of a Two Bladed Model Rotor to Evaluate the TAMI System in Descending Forward Flight," NASA CR-145195, May 1977.

[13]Rorke, J. B., Moffitt, R. C., and Ward, J. F., "Wind Tunnel Simulation of Full-Scale Vortices," American Helicopter Society 28th Annual National Forum, Washington, DC, May 1972.

[14]Balcerak, J. C., and Feller, R. F., " Effect of Sweep Angle on the Pressure Distribution and Effectiveness of the Ogee Tip in Diffusing a Line Vortex," NASA CR-132355, 1973.

[15]Chigier, N. A., and Corsiglia, V. R., "Tip-Vortices Velocity Distributions," American Helicopter Society 27th Annual National Forum, Washington, DC, May 1971.

[16]Balcerak, J. C., and Feller, R. F., "Vortex Modification by Mass Injection and by Tip Geometry Variation," U.S. Army Air Mobility Research and Development Lab., USAAMRDL TR-73-45, AD 771 966, June 1973.

[17]Mantay, W. R., Shidler, P. A., and Campbell, R. L., "Some Results of the Testing of a Full-Scale Ogee Tip Helicopter Rotor; Acoustics, Loads and Performance," AIAA Paper 77-1340, Oct. 1977.

[18]Brooks, T. M., Booth, E. R., Jr., Jolly, J. R., Jr., Yeager, W. T., Jr., and Wilbur, M. L., "Reduction of Blade-Vortex Interaction Noise through Higher Harmonic Pitch Control," *American Helicopter Society Journal*, Vol. 35, No. 1, 1990, pp. 86–91.

[19]Splettstoesser, W. R., Schultz, K. J., Kube, R., Brooks, T. F., Booth, E. R. Jr., Niesl, G., and Streby, O., "BVI Impulsive Noise Reduction by Higher Harmonic Pitch Control—Results of a Scaled Model Rotor Experiment in the DNW," Paper No. 91-61, 17th European Rotorcraft Forum, Berlin, Sept. 1991.

[20]Rai, M. M., "Navier-Stokes Simulation of Blade-Vortex Interaction Using High Order Accurate Upwind Schemes," AIAA Paper 87-0543, Jan. 1987.

[21]Rai, M. M., and Chaussee, D. S., "New Implicit Boundary Procedures: Theory and Application," *AIAA Journal*, Vol. 22, No. 8, 1984, pp. 1094–1100.

[22]Sculley, M. P., "Computation of Helicopter Rotor Wake Geometry and Its Influence on Rotor Harmonic Loads," MIT, ASRL TR-178-1, Cambridge, MA, March 1975.

[23]Darcy, H., "Les fontaines publiques de ville de Dijon," 1856, p. 590.

[24]Baldwin, B. S., and Lomax, H., "Thin-Layer Approximation and Algebraic Model for Separated Turbulent Flows," AIAA Paper 78-257, Jan. 1978.

[25]Launder, B. E., and Priddin, C. H., "A Comparison of Some Proposals for the Mixing Length Near a Wall," *International Journal of Heat and Mass Transfer*, Vol. 16, No. 3, 1973, pp. 700–702.

[26]Patankar, S. V., and Spalding, D. B., *Heat and Mass Transfer in Boundary Layers*, 2nd ed., International Text Co., London, 1970.

[27]Kays, W. M., and Crawford, M. E., *Convective Heat and Mass Transfer*, 2nd ed., McGraw-Hill, New York, 1980.

[28]Andersen, P. S., Kays, W. M., and Moffat, R. J., "Experimental Results for the Transpired Turbulent Boundary Layer in an Adverse Pressure Gradient," *Journal of Fluid Mechanics*, Vol. 69, Pt. 2, 1975, pp. 353–375.

[29]Chen, C. L., Chow, C. Y., Van Dalsem, W. R., and Holst, T. L., "Computation of Viscous Transonic Flow over Porous Airfoils," AIAA 25th Aerospace Sciences Meeting, AIAA Paper 87-0359, Reno, NV, Jan. 1987.

[30]Baker, R. J., Jonsson, V. K., and Launder, B. E., "The Turbulent Boundary Layer with Streamwise Pressure Gradient and Foreign-Gas Injection," Imperial College, Rept. ET/TN/G/31.

[31]Kays, W. M., and Moffat, R. J., *Studies in Convection*, Vol. 1, Academic Press, London, 1975.